Chinese Chemical Letters 37 (2026) 111001

Contents lists available at ScienceDirect

Chinese Chemical Letters

journal homepage: www.elsevier.com/locate/cclet

Interface effect induced electron-deficient Ni sites for efficient glycerol electrooxidation

Lan Tang[a], Ji Chen[a], Yucheng Wu[b], Linxin Qi[a], Xingyi Tian[a], Ming Li[a], Wenbin Wang[a,*], Rongxing He[a,*]

[a] Key Laboratory of Luminescence Analysis and Molecular Sensing, Ministry of Education, School of Chemistry and Chemical Engineering, Southwest University, Chongqing 400715, China
[b] Guangdong Provincial Key Laboratory of Fuel Cell Technology, School of Chemistry and Chemical Engineering, South China University of Technology, Guangzhou 510640, China

ARTICLE INFO

Article history:
Received 21 November 2024
Revised 3 February 2025
Accepted 25 February 2025
Available online 15 March 2025

Keywords:
Electron-deficient site
Heterojunction interface
Formate
Glycerol electrooxidation
High selectivity

ABSTRACT

Glycerol oxidation reaction has got lots of attention in an electrocatalytic system of simultaneous hydrogen production and valuable chemicals generation. However, the lack of electrochemical dehydrogenation capability of the active phase is hard to deliver a large current density at a low potential. Furthermore, high selectivity of products is also still far from being completed due to the adsorption-desorption disequilibrium of glycerol and the obtained products, reducing the economic feasibility and limiting the practical application. Here, we propose a strategy to boost the electrocatalytic glycerol oxidation through electron-deficient Ni sites induced by electron transfer of heterojunction interface. Taking Ni_3S_2/Cu_2S as a pre-catalysts, we demonstrate that the electron-deficient Ni site can favor the dehydrogenation of the active phase to facilitate the rapid transformation of Ni^{2+}/Ni^{3+} in the electrooxidation process of glycerol. Furthermore, electron deficient Ni sites balance competitive adsorption of active species, improving the activity and selectivity of glycerol oxidation. As expected, the electrocatalysts exhibit selectivity of 93.3 % for formate at the 1.35 V, and require only 1.45 V to drive an industrial-level current densities of 600 mA/cm^2. This work provides valuable insights into constructing highly active and selective electrocatalysts for organic electrosynthesis in hybrid water electrolysis.

© 2026 Published by Elsevier B.V. on behalf of Chinese Chemical Society and Institute of Materia Medica, Chinese Academy of Medical Sciences.

Currently, rapidly depleting fossil fuels and increasing environmental pollution make storage and conversion technologies of clean energy a priority [1–3]. Hydrogen, as a green energy source, is seen as an ideal alternative to traditional chemical fuels [4–7]. Electrocatalytic overall water splitting has attracted attention as a simple, low-cost mean of producing hydrogen [8–11]. However, the slow kinetics of the anodic oxygen evolution reaction (OER) in electrocatalytic overall water splitting limits the cathodic hydrogen production efficiency and significantly reduces energy utilization efficiency and economic feasibility [12–14]. Hydrogen production from hybrid electrolytic water, which utilizes electrocatalytic oxidation of small organic molecules to replace the OER, can not only reduce the energy consumption of hydrogen production but also realize the virtuous cycle of biomass [15–18]. Among various electrooxidation reactions of small organic molecules, glycerol oxidation reaction (GOR) is considered as a one of the ideal substitute for OER due to low onset potential [19–21]. Meanwhile, as the main product of GOR, formate has been used in the production of fine chemicals [22,23]. Therefore, coupling the GOR with the hydrogen evolution reaction (HER) is economically beneficial as it not only reduces the energy consumption for hydrogen production, but also allows for the simultaneous production of high value-added chemicals at the anode [24,25]. Great efforts have been devoted to developing advanced electrocatalysts for efficient glycerol electrooxidation [26,27], however, it is hard to achieve targeted selectivity for GOR products due to OER competition in anode and complex multi-electron transfer processes across multiple reaction pathways in GOR, limiting the economic potential of GOR [28,29].

Ni-based catalysts are currently one of the most potential non-precious metals for achieving high selectivity of glycerol oxidation products [30]. In GOR, Ni ions are oxidized to NiOOH by adsorbing OH^* and applying potentials, which serves as the active site for glycerol oxidation [31]. Upon contact with NiOOH, glycerol undergoes redox reactions, being oxidized to formate *etc.*, while NiOOH is reduced back to $Ni(OH)_2$. NiOOH is regenerated by the adsorp-

* Corresponding authors.
E-mail addresses: wangwenbin@swu.edu.cn (W. Wang), herx@swu.edu.cn (R. He).

https://doi.org/10.1016/j.cclet.2025.111001
1001-8417/© 2026 Published by Elsevier B.V. on behalf of Chinese Chemical Society and Institute of Materia Medica, Chinese Academy of Medical Sciences.

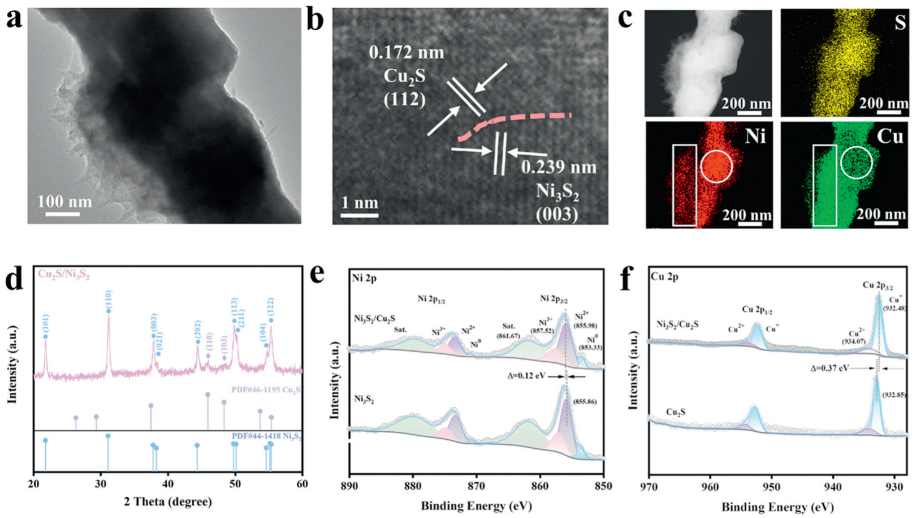


Fig. 1. Structural analysis of Ni_3S_2/Cu_2S. (a) TEM, (b) HRTEM and (c) HAADF-STEM images and the corresponding EDS element mapping of Ni_3S_2/Cu_2S. (d) XRD of Ni_3S_2/Cu_2S. (e) High-resolution Ni 2p XPS spectra of Ni_3S_2/Cu_2S and Ni_3S_2. (f) High-resolution Cu 2p XPS spectra of Ni_3S_2/Cu_2S and Cu_2S.

tion of OH* and applied potential, thus initiating a new cycle [32]. Therefore, promoting the generation and deprotonation of highly active phase is essential to improve the current density and product selectivity during GOR. In addition, it is worth noting that the catalytic process typically involves electron transfer and the adsorption and desorption of reactants and products on the catalyst surface, also affecting selectivity and large current density [33]. Apparently, the electrocatalytic performance of catalysts largely depends on the surface charge state of the constructed materials. Constructing heterointerfaces could effectively optimise the electronic structure of active sites in electrocatalysts and accelerate the charge transfer at the heterogeneous interface [34], thus possibly generate high content of metal hydroxide on the surface under oxidation conditions, providing multiple GOR active sites, as well as boosting the electrocatalytic performance [35,36].

Herein, we proposed interface effect induced electron-deficient Ni site for promoting *in situ* construction of $NiOOH/Cu(OH)_2$ heterojunction with SO_4^{2-} adsorption. Using Ni_3S_2/Cu_2S heterojunction as a pre-catalyst, it was confirmed that the electron-deficient Ni sites were more likely to form the highly active phase NiOOH due to the charge redistribution of the catalyst surface. During the GOR, in which Cu sites acted as an activator made electron-deficient Ni^{3+} active sites easier to deprotonate by reacting with nucleophilic reagents, promoting electrooxidation glycerol to formate. The electronic interaction of the two components at the heterogeneous interface facilitated generation of Ni^{3+} active species and accelerated the reversible conversion of $Ni^{2+} \leftrightarrow Ni^{3+}$ to improve electrochemical deprotonation of the active phase, enhancing the intrinsic activity of active sites. Density functional theory (DFT) calculation further revealed that the SO_4^{2-} adsorption promoted the loss of electrons at Ni sites. Besides, the electron-deficient Ni site balances the adsorption of the active species to boost activity and selectivity for GOR. Therefore, the catalysts required only 1.45 V to offer a 600 mA/cm^2 current density and showed a 93.3 % selectivity for formate at 1.35 V. This work shows that designing surface electronic structures through heterostructure is a promising strategy to enhance the catalytic performance of electrocatalysts in GOR.

The Ni_3S_2/Cu_2S supported on the Ni foam (Ni_3S_2/Cu_2S) was fabricated by simple hydrothermal method. The scanning electron microscopy (SEM) and transmission electron microscope (TEM) images show that the morphology of Ni_3S_2/Cu_2S is composed of curled wire-like nanobelts structures (Fig. 1a and Fig. S1 in Supporting information) [37]. High-resolution TEM (HRTEM) images present the distinct lattice fringe with 0.172 and 0.239 nm (Fig. 1b), corresponding to the (112) plane of Cu_2S and the (003) plane of Ni_3S_2, respectively. Interestingly, elemental mapping images show the uneven distribution of Ni and Cu elements in Ni_3S_2/Cu_2S, indicating that Ni_3S_2 and Cu_2S are randomly distributed in assembled heterostructure nanobelts (Fig. 1c) [38]. Furthermore, the X-ray diffraction (XRD) patterns confirm the coexistence of Ni_3S_2 and Cu_2S in Ni_3S_2/Cu_2S heterojunction (Fig. 1d). Obviously, the above results demonstrate that the Ni_3S_2/Cu_2S heterostructure nanosheets are successfully prepared. Meanwhile, Fig. S2 (Supporting information) shows that the Ni_3S_2 and Cu_2S as comparison samples were also successfully prepared. In addition, the chemical states of the Ni_3S_2/Cu_2S were further examined by X-ray photoelectron spectroscopy (XPS). As shown in Fig. 1e, the binding energy for Ni 2p in the Ni_3S_2/Cu_2S heterostructure exhibits a positive shift of 0.12 eV compared to that of Ni_3S_2, while the binding energy for Cu 2p in the Ni_3S_2/Cu_2S heterostructure has a negative shift of 0.37 eV with respect to that of Cu_2S (Fig. 1f). This implies that partial electrons transfer from Ni_3S_2 to Cu_2S at the heterointerface of Ni_3S_2/Cu_2S heterostructure, suggesting a decreasing electronic density for Ni atoms after the formation of Ni_3S_2/Cu_2S heterostructure. This local charge redistribution could adjust the surface electronic structure of Ni_3S_2/Cu_2S, expecting to facilitate the formation of active phase during reconstruction [39].

To evaluate the GOR performance for Ni_3S_2/Cu_2S, Ni_3S_2 and Cu_2S as a comparison were also carried out. The electrocatalytic OER performance of the Ni_3S_2/Cu_2S was explored in a 1 mol/L KOH electrolyte, while GOR performance was subsequently explored in 0.1 mol/L glycerol with 1 mol/L KOH electrolyte. As shown in Fig. 2a, the Ni_3S_2/Cu_2S exhibits higher GOR catalytic activity than that of OER. Particularly, at a current density of 100 mA/cm^2, the required potential for GOR is about 210 mV lower than that of OER. Meanwhile, the redox couples of Ni^{2+}/Ni^{3+} disappear, indicating more active Ni^{3+} is formed and the dehydrogenation ability of the Ni^{3+} is superior in GOR [30]. Furthermore, Ni_3S_2/Cu_2S exhibited much higher current density than Ni_3S_2 and Cu_2S (Fig. 2b). Especially, Ni_3S_2/Cu_2S requires only a low potential of 1.45 V (*vs.* RHE) to deliver an industrial-scale current density of 600 mA/cm^2, which current density at 1.45 V (*vs.* RHE) is three and seven times higher than Ni_3S_2 (208.8 mA/cm^2) and Cu_2S (79.5 mA/cm^2), respectively. Thus, these results confirm the promoting impact of the heterointerface. Moreover, Ni_3S_2/Cu_2S displays the smallest Tafel slope of

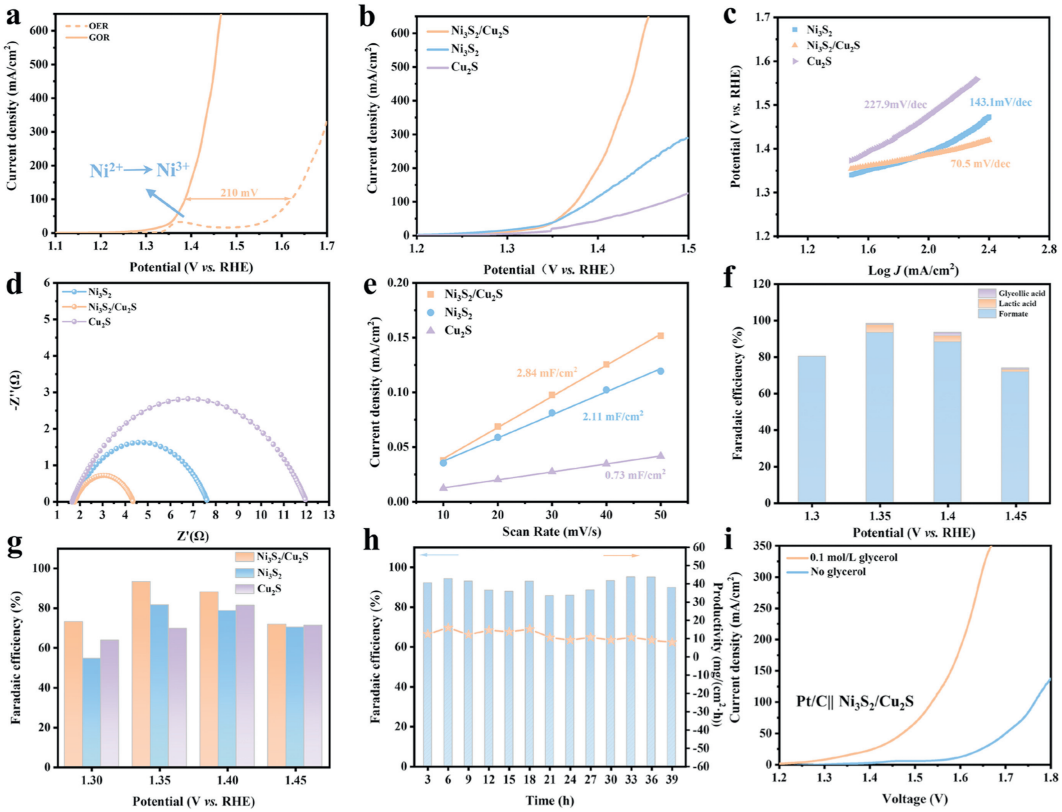


Fig. 2. Electrocatalytic glycerol oxidation performance. (a) LSV curves of Ni_3S_2/Cu_2S in 1 mol/L KOH with or without 0.1 mol/L glycerol electrolyte, (b) LSV curves of Ni_3S_2/Cu_2S, Ni_3S_2 and Cu_2S in 1 mol/L KOH with 0.1 mol/L glycerol electrolyte, (c) Tafel slopes, (d) EIS data, (e) C_{dl} values of Ni_3S_2/Cu_2S, Ni_3S_2 and Cu_2S, (f) FE of products for Ni_3S_2/Cu_2S, (g) FE of formate for Ni_3S_2/Cu_2S, Ni_3S_2 and Cu_2S, (h) FE and productivity of formate for the thirteen successive cycles, (i) LSV curves of Pt/C||Ni_3S_2/Cu_2S in 1 mol/L KOH with or without 0.1 mol/L glycerol electrolyte.

70.5 mV/dec (Fig. 2c), suggesting the fastest electronic transfer in comparison with Ni_3S_2 (143.1 mV/dec) and Cu_2S (227.9 mV/dec). Additionally, Ni_3S_2/Cu_2S also shows smaller charge-transfer resistance in 0.1 mol/L glycerol with 1 mol/L KOH electrolyte among studied samples by electrochemical impedance spectroscopy (EIS), suggesting the fast GOR kinetics of Ni_3S_2/Cu_2S (Fig. 2d). The electrochemical active surface area (ECSA) of electrocatalysts is an important parameter to affect catalytic performance. We used electrochemical double-layer capacitance (C_{dl}) to estimate the ECSA of Ni_3S_2/Cu_2S (Fig. 2e and Fig. S3 in Supporting information), reveals that the C_{dl} of Ni_3S_2/Cu_2S is 2.84 mF/cm^2, which is larger than that of Ni_3S_2 (2.11 mF/cm^2) and Cu_2S (0.73 mF/cm^2). These results suggest that Ni_3S_2/Cu_2S has more active sites, which is conductive to the improvement of GOR activity, indicating that the establishment of heterointerface between Ni_3S_2 and Cu_2S significantly enhances the electrocatalytic activity. The normalized LSV curves by ECSA (Fig. S4 in Supporting information) demonstrate the outstanding intrinsic activity of Ni_3S_2/Cu_2S for the GOR process. Expectedly, Ni_3S_2/Cu_2S possesses the highest turnover of frequency (TOF) of 2.16 s^{-1} (Fig. S5 in Supporting information), which is larger than that of Ni_3S_2 (1.87 s^{-1}) and Cu_2S (1.2 s^{-1}), confirming the highest intrinsic activity of Ni_3S_2/Cu_2S in the GOR process. Combined with the increase of active surface area, enhancement of the electrocatalytic glycerol oxidation activity of Ni_3S_2/Cu_2S could be attributed to the increased intrinsic activity and active surface area. In addition, the GOR performance of the catalyst powder samples was tested using a glassy carbon electrode, and Fig. S6 (Supporting information) shows that the heterojunction catalyst exhibits the better catalytic activity compared to the comparison sample. The selectivity of electrooxidation products and stability of catalysts are important evaluation indicators of catalysts for the organic's oxidation reaction. Therefore, ^{1}H NMR spectroscopy was implemented to probe the products obtained by electrolysis of the electrolyte at different potentials. As Fig. S7 (Supporting information) depicts, three peaks referring to formate, glycolic acid and lactic acid are yielded after GOR (performed at each given potentials), while the concentration of formate is much larger than glycolic acid and lactic acid, indicating that formate is the main product (Fig. 2f). At each applied potential, Ni_3S_2/Cu_2S presented higher productivity and Faraday efficiency (FE) for GOR to formate than Ni_3S_2 and Cu_2S (Fig. S8 in Supporting information and Fig. 2g). Obviously, the Ni_3S_2/Cu_2S exhibits FE values of 93.3 % for formate at 1.35 V, while Ni_3S_2 and Cu_2S only achieved FE of 81.7 % and 69.7 %. This result suggests that the Ni_3S_2/Cu_2S manifests excellent capability for C–C bond cleavage of glycerol. Upon the applied potential exceeding 1.4 V, the selectivity and FE of formate simultaneously reduce, which is due to overoxidation of formate or glycerol as well as the increasingly competitive OER. In addition, the glycerol oxidation stability of Ni_3S_2/Cu_2S is conducted at a constant potential of 1.35 V. As shown in Fig. 2h and Fig. S9 (Supporting information), the current density, productivity and FE of Ni_3S_2/Cu_2S are apparently unchanged under thirteen consecutive electrolysis cycles (39 h). To further investigate the promising Ni_3S_2/Cu_2S electrode for industrial production, a membrane-free hybrid electrolyzer with Ni_3S_2/Cu_2S as the anode and the Pt/C catalyst as the cathode immersed in the electrolyte of 1 mol/L KOH with 0.1 mol/L glycerol was constructed (Fig. 2i). The electrolyzer output a current density of 100 and 300 mA/cm^2 at the voltages of 1.53 and 1.64 V. Apparently, the required voltage at 100 mA/cm^2 for the cell is 235 mV lower than that of a pure water splitting electrolyzer. In addition, the FE of the GOR-HER coupled electrolyzer for formate production at the current density of 50–200 mA/cm^2 is above 80 % (Fig. S10

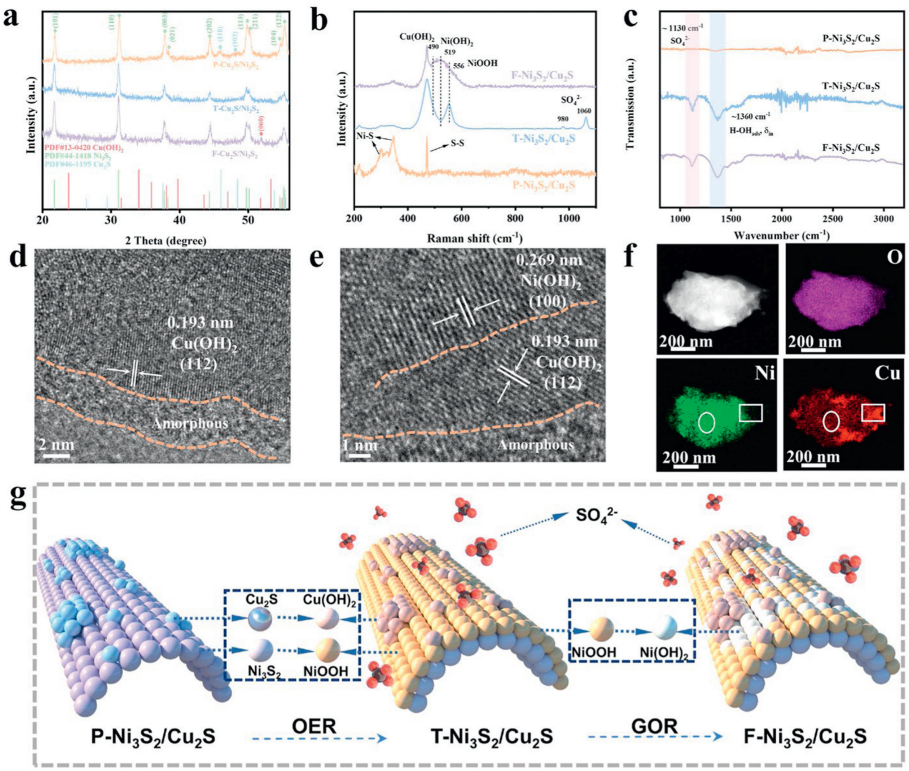


Fig. 3. The characterization of the Ni_3S_2/Cu_2S after OER (T-Ni_3S_2/Cu_2S) and GOR (F-Ni_3S_2/Cu_2S). (a) XRD patterns, (b) *ex-situ* Raman, (c) FT-IR of P-Ni_3S_2/Cu_2S, T-Ni_3S_2/Cu_2S and F-Ni_3S_2/Cu_2S. (d, e) HRTEM, (f) SAED image and the corresponding EDS element mapping of F-Ni_3S_2/Cu_2S. (g) Structure transformation diagram.

in Supporting information), which indicates that the electrolyzer has the potential for formate and hydrogen production simultaneously. These composite indicators suggest that Ni_3S_2/Cu_2S presents a comparable activity and selectivity for GOR among the reported NiCu-based GOR catalysts (Table S1 in Supporting information).

To understand the mechanisms for the enhanced activity of Ni_3S_2/Cu_2S in-depth, the realistic structure and chemical state of Ni_3S_2/Cu_2S after OER (T-Ni_3S_2/Cu_2S) and GOR (F-Ni_3S_2/Cu_2S) were investigated. As shown in Fig. 3a, the XRD pattern shows that the (110) and (103) planes of Cu_2S disappear after OER, while the presence of $Cu(OH)_2$ XRD signal after GOR, indicated that Cu_2S gradually transforms into $Cu(OH)_2$ during OER and GOR process. At the same time, the *ex-situ* Raman was done to complement the structural evolution of the catalyst (Fig. 3b). It revealed that both T-Ni_3S_2/Cu_2S and F-Ni_3S_2/Cu_2S exhibited characteristic peaks of $Cu(OH)_2$ at 490 cm^{-1} [40], but the signal of $Cu(OH)_2$ in F-Ni_3S_2/Cu_2S was stronger than that of T-Ni_3S_2/Cu_2S, which is consistent with the XRD result. The XRD and Raman results illustrate that the generation of $Cu(OH)_2$ during the GOR process. Interestingly, the Ni-S peak absented after OER and a new peak at 556 cm^{-1} appeared, which is ascribed to the NiOOH [41,42]. The NiOOH peak can be found to be weakening, while $Ni(OH)_2$ signal (519 cm^{-1}) enhances during GOR process [43], which confirms the NiOOH as the active phase for the oxidation of glycerol. Moreover, the clear SO_4^{2-} characteristic peaks (980 cm^{-1} and 1060 cm^{-1}) appear in the spectrum after OER [39,44], while it can be found that the signal of SO_4^{2-} disappears during the GOR process, which is due to the gradual desorption of SO_4^{2-} adsorbed on the catalyst surface during the surface construction process. The results of Fourier transform infrared (FT-IR) spectra showed that the absorption bands of SO_4^{2-} at 1130 cm^{-1} still existed in F-Ni_3S_2/Cu_2S (Fig. 3c) [45], confirming a little SO_4^{2-} ion adsorbed on the surface of the catalyst. In addition, after OER process, the catalyst still retains the wire-like nanobelts structures, but the nanobelts surface transformed into a needle-like nanostructure (Fig. S11 in Supporting information). Subsequently, the nanobelts structures were transformed into the nanosheets during the GOR process. (Fig. S12 in Supporting information). The HRTEM exhibited that the lattice fringe distances of 0.193 and 0.269 nm were according with the (112) lattice faces of $Cu(OH)_2$ and the (110) lattice faces of $Ni(OH)_2$ (Figs. 3d and e), respectively, while many amorphous phases were wrapping in the surface of nanosheets. Combined with Raman's results, the amorphous phase is considered to be NiOOH, as it is widely believed to be deeply involved in the GOR process, enhancing electrocatalytic activity [16,27]. Furthermore, the uneven distribution of Ni, Cu elements in F-Ni_3S_2/Cu_2S confirms that $Ni(OH)_2$, amorphous NiOOH and $Cu(OH)_2$ are randomly distributed in assembled heterostructure nanosheets (Fig. 3f). The random distribution of the reconstructed phases could keep the active Ni ion in an electron-deficient state through stabilizing interfacial charge transfer effect during the GOR process, favouring the electrochemical dehydrogenation of $Ni(OH)_2$ and the spontaneous dehydrogenation on NiOOH. In addition, amorphous NiOOH wrapped $Cu(OH)_2/Ni(OH)_2$ heterojunction with SO_4^{2-} adsorbing is a stable active phase for GOR (Figs. S13-S15 in Supporting information). Obviously, the surface of Ni_3S_2/Cu_2S was transformed into $NiOOH/Cu(OH)_2$ during OER process, while S^{2-} was oxidized to SO_4^{2-}, which was adsorbed on the catalyst surface. Subsequently, NiOOH acted as active phase for dehydrogenation and was reduced to $Ni(OH)_2$ during GOR process, thus the surface of T-Ni_3S_2/Cu_2S were further transformed into the amorphous NiOOH wrapped $Cu(OH)_2/Ni(OH)_2$ heterojunction (Fig. 3g).

To investigate the facilitating effect of electron-deficient Ni sites in heterostructure for the glycerol electrooxidation, the *in-situ* Raman was performed. As shown in Figs. 4a and b, two characteristic peaks at 472 and 556 cm^{-1} are observed at a potential of 1.15 V, which corresponding to the Ni–O vibration of NiOOH. When the potential was increased, these peaks were fading, implying that the Ni^{3+} species were active sites during GOR. However, characteristic peaks for NiOOH in T-Ni_3S_2/Cu_2S were not observed until

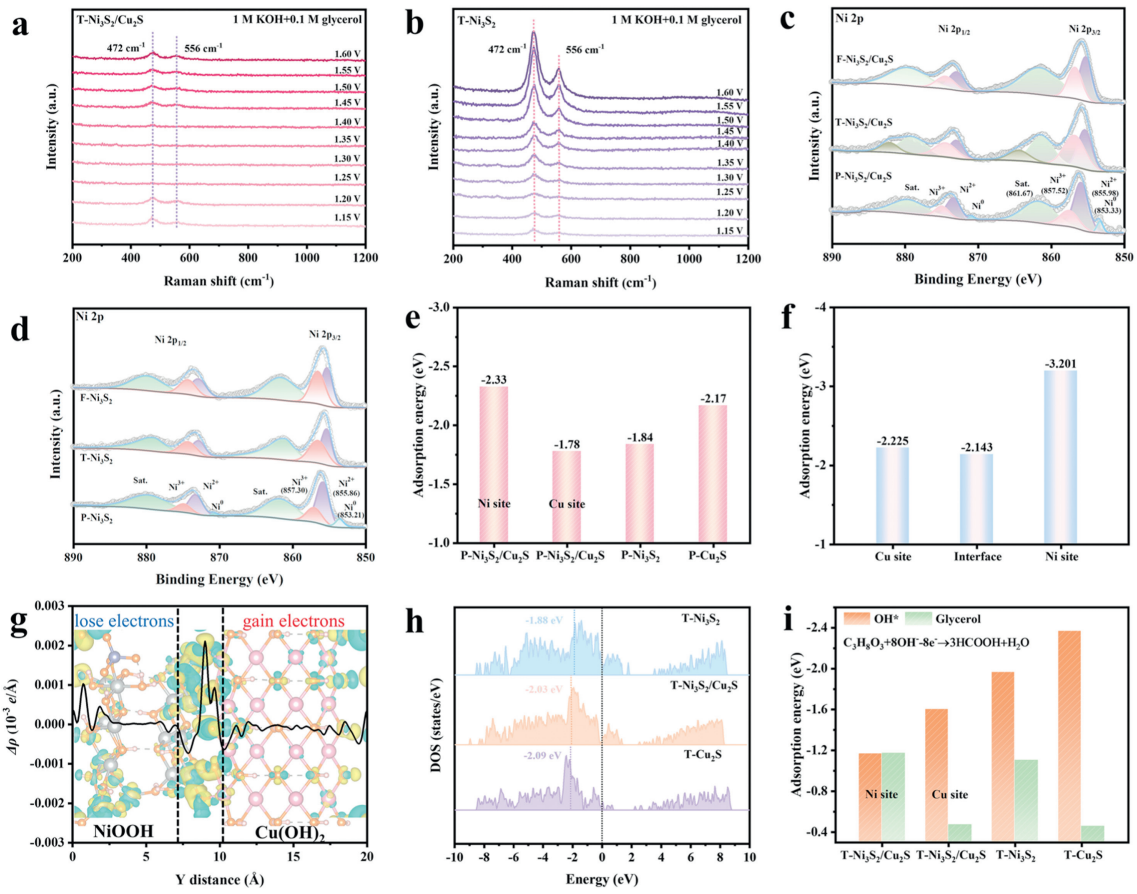


Fig. 4. Mechanism investigation. (a) *In situ* Raman of T-Ni_3S_2/Cu_2S during GOR. (b) *In situ* Raman of T-Ni_3S_2 during GOR. (c, d) High-resolution XPS spectra for Ni 2p. (e) Adsorption energy of OH^* on P-Ni_3S_2/Cu_2S (Ni site), P-Ni_3S_2/Cu_2S (Cu site), P-Ni_3S_2 and P-Cu_2S. (f) Adsorption energy of SO_4^{2-} at different sites in T-Ni_3S_2/Cu_2S. (g) Charge density difference. (h) DOS. (i) The calculated adsorption energy of glycerol and hydroxyl on samples.

the potential exceeded 1.45 V, implying that the electro-generated electron-deficient Ni^{3+} sites were rapidly reduced to Ni^{2+} by glycerol in a spontaneous reaction, while Ni^{2+} underwent electrochemical dehydrogenation to generate Ni^{3+} immediately (Fig. 4a). Thus, the heterojunction catalyst containing electron-deficient Ni achieved a rapid transformation equilibrium of Ni^{2+}/Ni^{3+}. When the potential exceeded 1.45 V, the NiOOH signal was monitored again because the limited amount of adsorbed glycerol could not completely consume NiOOH. However, as shown in Fig. 4b, the NiOOH signal enhanced at 1.30 V, which was earlier than that for T-Ni_3S_2/Cu_2S, indicating that the slow consumption and large accumulation of oxyhydroxides during glycerol oxidation. Hence, the active Ni ion in the electron-deficient state facilitates the reaction of glycerol with NiOOH in the GOR process, avoiding the accumulation of Ni^{3+}, resulting in improvement of performance. To further confirm the role of chemical state in F-Ni_3S_2/Cu_2S, F-Ni_3S_2 and F-Cu_2S, the XPS was employed. Apparently, through the OER pre-reconstructed process, the XPS characteristic peak of metallic Ni disappeared, and T-Ni_3S_2/Cu_2S obtained a higher content of Ni^{3+} than that of T-Ni_3S_2, suggesting that interface induce the generation of more electron-deficient Ni active sites (Figs. 4c and d, Figs. S16a and 17a in Supporting information). However, unlike the OER process, the Ni^{3+} contents of T-Ni_3S_2 and T-Ni_3S_2/Cu_2S were decreasing after GOR, which suggests that electrocatalytic mechanism of both T-Ni_3S_2 and T-Ni_3S_2/Cu_2S for GOR is consistent with the electrochemical dehydrogenation and spontaneous dehydrogenation mechanism. It is worth noting that the content of Ni^{3+} and M-O in F-Ni_3S_2/Cu_2S is less than that in F-Ni_3S_2 (Figs. 4c and d, Figs. S16a-c and S17a-c in Supporting information), indicating that T-Ni_3S_2/Cu_2S is more favorable to dehydrogenation in the self-adapted state. Moreover, it can be found that T-Ni_3S_2/Cu_2S and T-Cu_2S obtained high content of Cu^{2+} in OER, while the Cu^{2+} remained stable during the GOR process (Figs. S16d, S16e, S18a and S18b in Supporting information). As well as, compared with P-Cu_2S, both T-Cu_2S and F-Cu_2S possess more hydroxyl and less lattice oxygen suggesting that the Cu_2S evolved into $Cu(OH)_2$ after OER and GOR. (Figs. S18c and d in Supporting information). The high content of hydroxyl indicates that Cu_2S is hard to dehydrogenate, exhibiting insufficient GOR activity. Besides, the content of Cu^{2+} in T-Ni_3S_2/Cu_2S is less than that in T-Cu_2S, suggesting that the interfacial charge transfer promotes the Cu site to be an electron-rich state, result in it being difficult to activate. Combined with the enhancement of the $Cu(OH)_2$ peak in *ex-situ* Raman, it can be assumed that the active sites are mainly electron deficient Ni sites. Furthermore, it can be found that the signal of SO_4^{2-} gradually decreases after T-Ni_3S_2/Cu_2S, T-Ni_3S_2 and T-Cu_2S undergoing the GOR progress, which is consistent with the *ex-situ* Raman results (Figs. S16f, S17d and S18e in Supporting information). Based on the above results, Ni_3S_2/Cu_2S readily generate the active NiOOH during the reconstructed process due to the presence of electron-deficient Ni. In addition, the random distribution of the reconstructed phase stabilizes the electron transfer of the heterojunction interface, which keeps the active Ni ions in an electron-deficient state during the GOR process (Fig. S19 in Supporting information), which is conducive to the dehydrogenation for oxidizing the glycerol.

Density functional theory (DFT) calculation was established to demonstrate that electron-deficient Ni could promote the forma-

tion of active phase. It can be seen that the adsorption energy of OH* on P-Ni_3S_2/Cu_2S (Ni site) was enhanced due to the electron-deficient Ni sites, which promoted the formation of active phase in the reconstruction process (Fig. 4e). Considering that the reconstructed phase is adsorbed by only tiny amounts of the SO_4^{2-}, the adsorption energy of SO_4^{2-} were initially performed to illustrate the preferentially adsorbed sites. Obviously, the Ni sites present favorable adsorption capacity (Fig. 4f and Fig. S20 in Supporting information). Noticeably, Fig. 4g and Fig. S21 (Supporting information) exhibited the charge density distribution of the T-Ni_3S_2/Cu_2S and SO_4^{2-} adsorbing on the Ni site, showing that partial electron transferred from NiOOH to $Cu(OH)_2$. Meanwhile, partial electrons of NiOOH are also collected by SO_4^{2-}, thus enhancing the electron deficiency of the Ni site. The d-band center of T-Ni_3S_2/Cu_2S (−2.03 eV) is in a moderate position from the Fermi energy level, which compared to T-Cu_2S (−2.09 eV) and T-Ni_3S_2 (−1.88 eV) (Fig. 4h). Apparently, the T-Ni_3S_2/Cu_2S has a moderate adsorption strength for reaction intermediates, indicating that the surface sites of T-Ni_3S_2/Cu_2S have the potential to achieve the balance between adsorption and desorption capacity during GOR process [46,47]. Due to the competitive adsorption between OH* and glycerol, too strong adsorption of OH* is detrimental to the adsorption and activation of glycerol [48]. Therefore, balancing the competitive adsorption of glycerol and OH* is essential to improve the activity of GOR and the selectivity of the products [49]. In order to illustrate the enhancement of activity and selectivity, the adsorption energy of OH* and glycerol was calculated (Fig. 4i). Due to the weak adsorption of glycerol by T-Ni_3S_2/Cu_2S (Cu site), which could be considered that the electron-deficient Ni site is the main active site for GOR. The results of the glycerol adsorption energy on T-Ni_3S_2/Cu_2S (Ni site) showed that the glycerol adsorption capacity of T-Ni_3S_2/Cu_2S (Ni site) was enhanced relative to T-Ni_3S_2, and the strong adsorption of OH* got a large improvement, which balances the adsorption of OH* and glycerol, improving the activity and selectivity.

In summary, this work focuses on the ability of heterojunctions with electron-deficient Ni sites for the generation and rapid transformation of active phases, and achieves the regulation of selective adsorption of active species. The experimental characterizations confirmed that the electron-deficient Ni sites of Ni_3S_2/Cu_2S promote the generation of highly active phases during pre-oxidation process, leading to the formation of amorphous NiOOH/$Cu(OH)_2$ heterojunction with SO_4^{2-} adsorbing. The NiOOH/$Cu(OH)_2$ preserves the electron-deficient Ni sites, which make active phase more susceptible to dehydrogenation, accelerating the transformation of the active site during GOR process. Therefore, the heterojunction catalysts demonstrates an exceptionally low potential of 1.45 V to achieve a industrial-scale current density of 600 mA/cm^2 toward efficient glycerol oxidation reaction. Furthermore, we demonstrated that benefiting from the electron-deficient Ni sites balances the competing adsorption between the active species, the catalyst exhibits high selectivity of 93.3 % for formate, which exceed those of most of the reported NiCu-based catalysts. This work provides new insights into developing a NiCu-based heterojunction electrocatalysts with glycerol oxidation.

Declaration of competing interest

The authors declare that they have no known competing financial interest or personal relationships that could have appeared to influence the work reported in this paper.

CRediT authorship contribution statement

Lan Tang: Writing – original draft, Methodology, Conceptualization. **Ji Chen:** Methodology. **Yucheng Wu:** Software, Resources. **Linxin Qi:** Methodology. **Xingyi Tian:** Methodology. **Ming Li:** Resources. **Wenbin Wang:** Writing – review & editing, Investigation, Funding acquisition. **Rongxing He:** Writing – review & editing, Software, Resources.

Acknowledgments

This work was financially supported by the National Natural Science Foundation of China (No. 22305193), the Natural Science Foundation of Chongqing (No. CSTB2023NSCQ-MSX0690), the Fundamental Research Funds for the central Universities (Nos. SWU-KQ22048, SWU-XDJH202314), the Innovation Research 2035 Pilot Plan of Southwest University (No. SWU-XDZD22011), the Chongqing Research and Innovation Fund for postgraduate students (No. CYS23189). We also acknowledge technical support from Analytical and Testing Center in Southwest University.

Supplementary materials

Supplementary material associated with this article can be found, in the online version, at doi:10.1016/j.cclet.2025.111001.

References

[1] K.A. Adegoke, A.K. Oyebamiji, A.O. Adeola, et al., Coord. Chem. Rev. 517 (2024) 215959.
[2] S. Xiao, Q. Fu, Z. Li, et al., Renew. Sust. Energ. Rev. 150 (2021) 111375.
[3] Y. Pan, H. Zhang, B. Zhang, et al., Nat. Commun. 14 (2023) 1013.
[4] Y. Huang, X. Chong, C. Liu, et al., Angew. Chem. Int. Ed. 57 (2018) 13163–13166.
[5] D. Li, H. Cheng, X. Hao, et al., Adv. Mater. 36 (2023) 2304917.
[6] H. Yu, W. Wang, Q. Mao, et al., Appl. Catal. B: Environ. 330 (2023) 122617.
[7] P. Zhai, C. Wang, Y. Zhao, et al., Nat. Commun. 14 (2023) 1873.
[8] J. Liu, W. Du, S. Guo, et al., Adv. Sci. 10 (2023) 2300717.
[9] M. Hou, L. Zheng, D. Zhao, et al., Nat. Commun. 15 (2024) 1342.
[10] W. Wang, Q. Wen, D. Huang, et al., Angew. Chem. Int. Ed. (2024) e202415132.
[11] X. Chen, X. Li, Y. Peng, et al., Adv. Funct. Mater. 35 (2025) 2416091.
[12] X. Zheng, Y. Cao, Z. Wu, et al., Adv. Energy Mater. 12 (2022) 2400851.
[13] M. Lin, M. Gu, X. Deng, et al., Chem. Eng. J. 468 (2023) 143705.
[14] S. Sun, X. Zhou, B. Cong, et al., ACS Catal. 10 (2020) 9086–9097.
[15] P. Zhu, Y. Shen, Z.-M. Zhang, et al., ACS Catal. 14 (2024) 7674–7683.
[16] Y. Lin, Y. Chen, H. Ren, et al., Adv. Funct. Mater. 34 (2024) 2404594.
[17] H. Huang, C. Yu, X. Han, et al., Energy Environ. Sci. 13 (2020) 4990–4999.
[18] W. Wang, Y. Wang, R. Yang, et al., Angew. Chem. Int. Ed. 59 (2020) 16974–16981.
[19] Z. Xia, C. Ma, Y. Fan, et al., ACS Catal. 14 (2024) 1930–1938.
[20] J. Li, X. Meng, X. Song, et al., Adv. Funct. Mater. 34 (2024) 2316718.
[21] X. Wu, Y. Xie, R. Deng, et al., ACS Appl. Mater. Inter. 16 (2024) 5905–5914.
[22] W. Luo, H. Tian, Q. Li, et al., Adv. Funct. Mater. 34 (2023) 2306995.
[23] L. Fan, Y. Ji, G. Wang, et al., J. Energy Chem. 72 (2022) 424–431.
[24] W. Tang, L. Zhang, T. Qiu, et al., Angew. Chem. Int. Ed. 62 (2023) e202305843.
[25] C. Li, H. Li, B. Zhang, et al., Angew. Chem. Int. Ed. 63 (2024) e202411542.
[26] J. Ma, X. Wang, J. Song, et al., Angew. Chem. Int. Ed. 63 (2024) e202319153.
[27] L. Ma, Y. Miao, J. Yang, et al., Adv. Energy Mater. 14 (2024) 2401061.
[28] Y. Zhu, Q. Qian, Y. Chen, et al., Adv. Funct. Mater. 33 (2023) 2300547.
[29] Y. Zheng, Z. Kang, H. Li, et al., Adv. Funct. Mater. 35 (2025) 2412810.
[30] L. Xu, Y. Yang, C. Li, et al., Chem. Eng. J. 481 (2024) 148304.
[31] M.K. Goetz, M.T. Bender, K.S. Choi, Nat. Commun. 13 (2022) 5848.
[32] W. Chen, C. Xie, Y. Wang, et al., Chem 6 (2020) 2974–2993.
[33] G. Ren, B. Liu, X. Xu, et al., Nano Today 56 (2024) 102315.
[34] Y. Wang, J. Huang, Y. Chen, et al., J. Colloid Interface Sci. 672 (2024) 12–20.
[35] Y. Zhou, B. Chu, Z. Sun, et al., Appl. Catal. B: Environ. Energy 323 (2023) 122168.
[36] B. Huang, J. Wang, D. Xie, et al., Chem. Eng. J. 498 (2024) 155006.
[37] X. Zhang, Z. Chen, M. Jiao, et al., Appl. Catal. B: Environ. Energy 279 (2020) 119383.
[38] Q. Ji, Y. Kong, H. Tan, et al., ACS Catal. 12 (2022) 4318–4326.
[39] Q. Gou, Y. Mao, S. Lv, et al., Appl. Catal. B: Environ. Energy 348 (2024) 123810.
[40] Y. Deng, A.D. Handoko, Y. Du, et al., ACS Catal. 6 (2016) 2473–2481.
[41] X. Liu, J. Wang, H. Liao, et al., Nano Lett. 23 (2023) 5027–5034.
[42] F. Li, Y. Li, L. Li, et al., Chem. Sci. 13 (2022) 9256–9264.
[43] H. Ze, Z.L. Yang, M.L. Li, et al., J. Am. Chem. Soc. 146 (2024) 12538–12546.
[44] M. Chen, Y. Zhang, R. Wang, et al., J. Energy Chem. 84 (2023) 173–180.
[45] Y. Lin, J. Fang, W. Wang, et al., Adv. Energy Mater. 13 (2023) 2300604.
[46] Y. Yu, Y. Wu, W. Luo, et al., Chem. Eng. J. 477 (2023) 147076.
[47] Y. Hu, M. Tu, T. Xiong, et al., J. Energy Chem. 103 (2025) 282–293.
[48] S. Zhong, B. He, S. Wei, et al., Appl. Catal. B: Environ. Energy 362 (2025) 124743.
[49] D. Xiao, X. Bao, D. Dai, et al., Adv. Mater. 35 (2023) 202304133.